Inorganic Chemistry

pubs.acs.org/IC Article

# Two Polymorphs of $BaZn_2P_2$: Crystal Structures, Phase Transition, and Transport Properties

Adam Balvanz, Sviatoslav Baranets, Michael O. Ogunbunmi, and Svilen Bobev*

Cite This: https://doi.org/10.1021/acs.inorgchem.1c02209 Read Online

ACCESS | Metrics & More | Article Recommendations | Supporting Information

**ABSTRACT:** The novel $\alpha$-$BaZn_2P_2$ structural polymorph has been synthesized and structurally characterized for the first time. Its structure, elucidated from single crystal X-ray diffraction, indicates that the compound crystallizes in the orthorhombic $\alpha$-$BaCu_2S_2$ structure type, with unit cell parameters $a$ = 9.7567(14) Å, $b$ = 4.1266(6) Å, and $c$ = 10.6000(15) Å. With $\beta$-$BaZn_2P_2$ being previously identified as belonging to the $ThCr_2Si_2$ family and with the precedent of structural phase transitions between the $\alpha$-$BaCu_2S_2$ type and the $ThCr_2Si_2$ type, the potential for the pattern to be extended to the two different structural forms of $BaZn_2P_2$ was explored. Thermal analysis suggests that a first-order phase transition occurs at ~1123 K, whereby the low-temperature orthorhombic $\alpha$-phase transforms to a high-temperature tetragonal $\beta$-$BaZn_2P_2$, the structure of which was also studied and confirmed by single-crystal X-ray diffraction. Preliminary transport properties and band structure calculations indicate that $\alpha$-$BaZn_2P_2$ is a p-type, narrow-gap semiconductor with a direct bandgap of 0.5 eV, which is an order of magnitude lower than the calculated indirect bandgap for the $\beta$-$BaZn_2P_2$ phase. The Seebeck coefficient, $S(T)$, for the material increases steadily from the room temperature value of 119 $\mu$V/K to 184 $\mu$V/K at 600 K. The electrical resistivity of $\alpha$-$BaZn_2P_2$ is relatively high, on the order of 40 m$\Omega$·cm, and the $\rho(T)$ dependence shows gradual decrease upon heating. Such behavior is comparable to those of the typical semimetals or degenerate semiconductors.

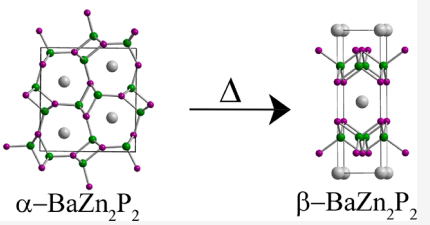


## INTRODUCTION

Over the past decade, there has been a considerable research effort into synthesizing and characterizing Zintl compounds within the $M$–Zn–$Pn$ (M = Ca, Sr, Ba, Eu, and Yb; $Pn$ = P, As, Sb, and Bi) ternary phase spaces. The results of these inquires have been documented in many papers on the realization of both of unusual properties[1−5] and structures.[6−16] Under this broad umbrella of compounds that have been explored, perhaps the most substantial effort has been dedicated to researching "1−2−2" phases—one of the most abundant groups of ternary Zintl compounds. Compounds with general formulas $MX_2Pn_2$ are known to form in a variety of structure types, encompassing a large range of elemental compositions (X = metal in a divalent state). The majority of these compounds crystallize in the well-known and thoroughly studied $ThCr_2Si_2$ structure type,[17] which most notably includes a class of iron arsenide unconventional superconductors. The $CaAl_2Si_2$ type is also another well-studied class[18] within the "1−2−2" family, which include several compounds with great potential for thermoelectric applications.[18−20] While the majority of these "1−2−2" structures crystallize in one of the above-mentioned structure types, there are still other less common types as well, including $BaNi_2Ge_2$[21] and $\alpha$-$BaCu_2S_2$.[22] The latter structure type is known for only two pnictides, which were first published more than four decades ago, both of which contained Ba and Zn:[23,24] $BaZn_2As_2$ and $BaZn_2Sb_2$.

Among these structures, within the wide range of structure types, there are also a plethora of observed structural phase transitions that have been identified, with a great number of them involving compounds within the $ThCr_2Si_2$ structure type. Such transitions in this type have been categorized previously,[17] but the broad trends regarding these transitions will be restated here for brevity. A significant number of the identified structural phase transitions have been induced by pressure,[25−29] causing a collapse of the featured polyanionic layers in the $ThCr_2Si_2$ structure type. However, there are also a number of phase transitions that are initiated based on changes in temperature, which instead causes a structural distortion, forming a compound with a different overall global structure and symmetry. Specifically, the transition between the $\alpha$-$BaCu_2S_2$ and $ThCr_2Si_2$ is one of these temperature-induced transitions and is rare, yet repeatable with $BaZn_2As_2$,[1] $BaCu_2S_2$,[30] and $BaAl_2Ge_2$[31] displaying such a transition between structures within those two specific structure types. Furthermore, within this small group of compounds, there are still some variances because while the reported transition for $BaCu_2S_2$ was identified as being irreversible, the transition displayed by $BaAl_2Ge_2$ was reported to be reversible, indicating interesting structural rearrangement occurring between these two structure types.

Received: July 21, 2021


© XXXX American Chemical Society

One should also recall that the $\alpha$-$BaCu_2S_2$ and $ThCr_2Si_2$ structure types not only contain several compounds that undergo structural phase transitions but also show interesting thermoelectric properties. The $\alpha$- and $\beta$-polymorphs of $BaZn_2As_2$ as well as their K-doped counterparts, for instance, have been the subject of recent investigations based on each compound's potential for thermoelectric applications.[1,32] $BaZn_2Sb_2$, crystallizing in the $\alpha$-$BaCu_2S_2$ structure type, has also been the subject of research efforts looking into the thermoelectric potential[33] and doping optimization[34] of the compound. With different crystal chemistry occurring for compounds crystallizing with Bi within their crystal structures,[35] it is clear that the P analogues of these "1−2−2" phases are worthy of exploration based on their interesting structures and their potential for high thermoelectric merit.

In this study, we present the synthesis and structural description for the newly synthesized $\alpha$-$BaZn_2P_2$ orthorhombic "1−2−2" structural modification, crystallizing in the $\alpha$-$BaCu_2S_2$ structure type, as well as revised synthesis and structural description for the $\beta$-$BaZn_2P_2$ polymorph, which crystallizes in the well-known $ThCr_2Si_2$ structure type (although commonly termed being its own structure type). As a result of these synthetic experiments, we have identified a structural phase transition between the two polymorphs that is induced at high temperatures. Such types of transitions are rare, with only three other documented dimorphic cases involving these specific structure types thus far.[1,30,31] $\alpha$- and $\beta$-$BaZn_2P_2$ appear to be the only phosphorus-containing phases that exhibit this phenomenology. We also present preliminary transport property measurements, including thermopower and high-temperature resistivity, on single crystals of the low-temperature orthorhombic polymorph of $BaZn_2P_2$ only. The measured values for thermopower and theoretical electronic structure indicate that $\alpha$-$BaZn_2P_2$ is a p-type semiconductor ($E_g \approx 0.5$ eV) with holes as the primary charge carrier.

## EXPERIMENTAL SECTION

**Synthesis.** All procedural steps and manipulations were performed either in a argon-filled glovebox or under vacuum. The elements (Ba, Zn, P, Pb) used for the synthesis of the title compounds were sourced from either Sigma-Aldrich or Alfa Aesar and had a stated purity of greater than 99.9 wt % and were used as received. Reactions were performed either in standard, 2 $cm^3$ high-purity alumina crucibles or in custom-made 3/8 in. (OD) niobium crucibles; the latter were manufactured by sealing one end of open tubes. The vessels were then flame-sealed in a silica jacket and loaded into a high-temperature muffle furnace for programmed heat treatment.

The two polymorphs of $BaZn_2P_2$ were both originally synthesized by using molten lead as a solvent (flux). The Pb-flux technique calls for the elements in desired stoichiometric ratios to be placed into suitable crucibles. A large amount of Pb, typically in 10-fold or greater excess, was then added. Lead melts at low temperature and dissolves the reactants. The structure crystallizing in the *Pnma* space group (termed $\alpha$-$BaZn_2P_2$ in further discussion) was first isolated from a reaction designed to produce the Zn-containing analogue of the earlier synthesized $Ba_3Cd_2P_4$ phase.[36] As such, the elements were loaded with the ratio 3:2:4:15 for Ba, Zn, P, and Pb, respectively. After being placed into a sealed silica jacket, the reaction vessel was placed into the furnace, heating to a peak temperature of 1173 K for 24 h, and then slowly cooled (2 K/h) to 823 K. Once the final temperature was reached, the silica ampule was removed from the furnace and centrifuged at high speeds to remove the excess Pb flux. Crystals of what turned out to be $\alpha$-$BaZn_2P_2$ were then isolated; they formed as thin, black needles/thin rods. However, the sample was not phase pure, so subsequent adjustments to the reaction conditions, specifically the nominal stoichiometry, were made to maximize the yield (Figure S1).

The high-temperature $BaZn_2P_2$ polymorph, crystallizing in the tetragonal crystal system (termed $\beta$-$BaZn_2P_2$ in further discussion), was not identified as a product of the reaction mentioned above. Further optimization of the reaction parameters, when Ba, Zn, P, and Pb were taken with the stoichiometric ratios 1:2:2:10, respectively, at peak temperature 1273 or 1373 K, while still slowly cooling (2−3 K/h) to 923−823 K, produced $\beta$-$BaZn_2P_2$ in variable amounts. There appeared to be little control over the ratio of the two polymorphs as similar reactions could produce a sample of primarily either the $\alpha$- or $\beta$-phase. It is also important to note there that the crystals of the $\beta$ phase that were produced proved to be of suitable quality for single crystal X-ray diffraction experiments but were of insufficient size for property measurements. The best synthetic route to obtaining a bulk sample of the high-temperature phase, though, was found to be annealing a sample that contained a mixture of the two polymorphs in a furnace at 1123 K for an extended period and then quenching the sample in cold water (Figure S2). Such a reaction effectively produced high amounts of $\beta$-$BaZn_2P_2$ with little $\alpha$-$BaZn_2P_2$ impurity even when the original sample was primarily the $\alpha$-polymorph (Figure S3).

Direct reactions of Ba, Zn, and P were not tried as a part of this study. Reactions exploring Sn flux were pursued, at the same conditions as those in Pb flux, and yielded small crystals of $\alpha$-$BaZn_2P_2$ together with some other Ba−Sn−P phases.

**X-ray Powder Diffraction.** The single-crystalline products that were synthesized as a result of these experiments were finely ground inside an argon-filled glovebox until the resulting material resembled a powder-like consistency. A Rigaku Miniflex powder diffractometer operated inside the glovebox was used for the measurements. The tabletop diffractometer utilizes filtered Cu K$\alpha$ radiation ($\lambda$ = 1.5418 Å). Powder diffraction patterns were collected at room temperature by using a $\theta$−$\theta$ mode covering the range 5°−75° with a step of 0.05°/step and an exposure time of 2 s/step.

Diffraction experiments were also used monitor the stability of the title compounds in the ambient environment. The ground materials were left inside a fume hood for 48 h, and then the powder diffraction data were recollected. After 2 days in an ambient environment, there was little difference in diffraction intensity, indicating that both materials are air stable within the window of time explored.

**Single-Crystal X-ray Diffraction.** Crystals of the title compounds that were of suitable size and quality were selected inside an argon-filled glovebox, and then cut to size under an optical microscope, by using a bath of Paratone-N oil. The selected crystals were then scooped with a MiTeGen plastic loop and placed onto the goniometer of a Bruker Apex-II CCD diffractometer. A Mo K$\alpha$ radiation source (0.71073 Å) was utilized for the diffraction experiment. During the data collection, a constant temperature of 200 K was maintained by a built-in cooling system using cold $N_2$ vapor, which was generated through evaporation of the liquid. The cold $N_2$ stream served to also harden the Paratone-N oil surrounding the crystal, such that an inert environment was preserved during diffraction.

Data were collected, integrated, and corrected for absorption by using software supplied by Bruker.[37,38] The structures were solved by using ShelXT,[39] utilizing Olex2 as a graphical interface.[40] Refinements of the solved structure were performed by using a full-matrix least-squares method on $F^2$ as implemented in SHELXL.[41] Important crystallographic information and refinement parameters can be found in Table 1. The refined atomic coordinates and equivalent displacement parameters are tabulated in Table 2. A listing of selected interatomic distances is given in Table S1 of the Supporting Information.

**Thermopower and High-Temperature Resistivity.** Thermopower and transport property measurements were conducted on $\alpha$-$BaZn_2P_2$ only, since the synthesized $\beta$-$BaZn_2P_2$ crystals were not of suitable size. Measurement of the Seebeck coefficient was done within the temperature range 300−620 K. We collected the data with the MMR-Tech. SB-100 module using the integral method and a constantan wire as a reference material. A temperature variable


https://doi.org/10.1021/acs.inorgchem.1c02209
Inorg. Chem. XXXX, XXX, XXX−XXX

**Table 1. Selected Crystallographic Data and Refinement Parameters for the Two Polymorphs of $BaZn_2P_2$**

| empirical formula | $\alpha$-$BaZn_2P_2$ | $\beta$-$BaZn_2P_2$ |
|---|---|---|
| fw (g mol$^{-1}$) | 330.02 | |
| radiation source | Mo K$\alpha$, $\lambda$ = 0.71073 Å | |
| temperature (K) | 200 ± 2 | |
| crystal system | orthorhombic | tetragonal |
| space group | *Pnma* (no. 62) | *I*4/*mmm* (no. 139) |
| *Z* | 4 | 2 |
| *a* (Å) | 9.7567(14) | 4.037(3) |
| *b* (Å) | 4.1266(6) | 4.037(3) |
| *c* (Å) | 10.6000(15) | 13.260(10) |
| *V* (Å$^3$) | 426.78(11) | 216.1(3) |
| $\rho_{calc}$ (g cm$^{-3}$) | 5.14 | 5.07 |
| $\mu$ (cm$^{-1}$) | 208.0 | 205.3 |
| $R_1$ ($I > 2\sigma_I$)[a] | 0.0162 | 0.0221 |
| $R_1$ (all data) | 0.0203 | 0.0224 |
| $wR_2$ ($I > 2\sigma_I$)[1] | 0.0329 | 0.0506 |
| $wR_2$ (all data) | 0.0347 | 0.0508 |
| largest peak/deepest hole (e$^-$/Å$^3$) | 0.72/−0.90 | 1.83/−0.73 |

[a] $R_1 = \sum||F_o| - |F_c||/\sum|F_o|$; $wR_2 = [\sum[w(F_o^2 - F_c^2)^2]/\sum[w(F_o^2)^2]]^{1/2}$, where $w = 1/[\sigma^2F_o^2 + (AP)^2 + (BP)]$, and $P = (F_o^2 + 2F_c^2)/3$; *A* and *B* are the weight coefficients.

**Table 2. Fractional Atomic Coordinates and Equivalent Displacement Parameters ($U_{eq}$)[a] for $\alpha$-$BaZn_2P_2$ and $\beta$-$BaZn_2P_2$**

| atom | site | symmetry | *x* | *y* | *z* | $U_{eq}$/Å$^2$ |
|---|---|---|---|---|---|---|
| | | | $\alpha$-$BaZn_2P_2$ | | | |
| Ba | 4*c* | *m* | 0.2468(1) | 1/4 | 0.3260(1) | 0.007(1) |
| Zn1 | 4*c* | *m* | 0.0484(1) | 1/4 | 0.6154(1) | 0.008(1) |
| Zn2 | 4*c* | *m* | 0.0976(1) | 1/4 | 0.0509(1) | 0.008(1) |
| P1 | 4*c* | *m* | 0.4799(1) | 1/4 | 0.6603(1) | 0.006(1) |
| P2 | 4*c* | *m* | 0.3486(1) | 1/4 | 0.0399(1) | 0.006(1) |
| | | | $\beta$-$BaZn_2P_2$ | | | |
| Ba | 2*a* | 4/*mmm* | 0 | 0 | 0 | 0.016(1) |
| Zn | 4*d* | $\bar{4}$*m*2 | 0 | 1/2 | 1/4 | 0.014(1) |
| P | 4*e* | 4*mm* | 0 | 0 | 0.3606(2) | 0.013(1) |

[a] $U_{eq}$ is defined as one-third of the trace of the orthogonalized $U_{ij}$ tensor.

chamber was employed to house the crystal, which was mounted to a ceramic stage through the use of high-purity silver paint. An inert atmosphere was maintained during the measurement by evacuating the chamber to ∼10 mTorr.

High-temperature resistivity was measured within a temperature window of 300−400 K by using a H-50 module sourced from MMR Tech. Measurements were made through the four-probe Van der Pauw method on the plate-like sample with the thickness of ca. 80 $\mu$m, utilizing four platinum wires and high-purity silver paint to make contacts. The same temperature variable chamber was used, and an inert environment was maintained throughout the experiment through the presence of a vacuum (*vide supra*).

**Thermal Analysis.** Thermogravimetric/differential scanning calorimetry (TG/DSC) experiments were conducted by using a TA Instruments SDT Q600. Analysis was conducted on samples of primarily $\alpha$-$BaZn_2P_2$ with ca. 10−30 mg in mass, which was loaded into a high-purity alumina pan for analysis. Following a brief equilibration period at 323 K, the sample was heated to 1223 K at a rate of 20 K/h. The sample was then cooled to 523 K at the same ramp rate. An inert atmosphere was maintained by a constant flow (100 mL/min) of high-purity argon (Grade 5.0) gas.

**First-Principles Electronic Structure Calculations.** The electronic structure data were calculated for both polymorphs of $BaZn_2P_2$, within the density functional theory framework (DFT), by using the TB-LMTO-ASA code.[42] The local density approximation (LDA) was utilized through the von Barth−Hedin implementation.[43] Integrations in the *k*-space were performed through the tetrahedron method, by using a *k*-mesh of 1280 and 5408, in the Brillouin zone, for $\alpha$-$BaZn_2P_2$ and $\beta$-$BaZn_2P_2$, respectively. Empty spheres were introduced as a necessary step such that the atomic sphere approximation (ASA) was fulfilled. The basis set for both compounds was composed of the following: the 6s, (6p), 5d, and 4f orbitals of Ba; the 4s, 4p, and 3d orbitals for Zn; and the 3s, 3p, and (3d) orbitals of P. The orbitals in parentheses were downfolded and treated by using the Löwdin technique. The calculations made use of the experimentally determined unit cell parameters and atomic coordinates (Tables 1 and 2). The reference energy was selected to be the Fermi energy ($E_F$ = 0 eV). The chemical bonding analysis was conducted for the filled electronic states by calculation of the energy contribution for selected atom pairs by using the Crystal Orbital Hamilton Population (COHP) method, as implemented in the TB-LMTO-ASA code.[44]

## RESULTS AND DISCUSSION

**Crystal Structure of Two $BaZn_2P_2$ Polymorphs.** Both the $\alpha$-$BaZn_2P_2$ and $\beta$-$BaZn_2P_2$ polymorphs crystallize in previously identified structure types. Yet, the unexpected discovery of $\alpha$-$BaZn_2P_2$ as well as the enhanced and challenging single-crystal diffraction work on $\beta$-$BaZn_2P_2$ warrants a brief discussion of each crystal structure as a part of this presentation. The two structures will be the subject of the discussion within this section.

**$\alpha$-$BaZn_2P_2$.** There are five independent atomic positions in the asymmetric unit of the $\alpha$-$BaZn_2P_2$ structure, with Zn and P atoms having two unique sites and one for the Ba atom. Each atom, though, is located in a Wyckoff site *c* with mirror symmetry (Table 2). The elucidated crystallographic parameters classify $\alpha$-$BaZn_2P_2$ as isotypic to $\alpha$-$BaCu_2S_2$.[22] Within the same structure type (Pearson symbol *oP*20) there are only Ba-containing phases; two other pnictides, $BaZn_2Pn_2$ (*Pn* = As and Sb),[23,24] are also known, in addition to several chalcogenides $BaCu_2Ch_2$ (*Ch* = S, Se, and Te)[22,45] and tetrelides $BaAl_2Tt_2$ (*Tt* = Si and Ge).[31,46]

The specific structural elements of compounds within the $\alpha$-$BaCu_2S_2$ structure type have been known for over 4 decades; however, we revisit the structural description here since $\alpha$-$BaZn_2P_2$ is the first pnictogen-containing material to this join the group since the late 1970s.

The Zn atoms present in the structure are coordinated to four P atoms in the form of distorted tetrahedra, i.e., the distances varying between 2.4305(7) and 2.551(1) Å for Zn1−P bonds and 2.452(1) and 2.518(1) Å for Zn2−P bonds, respectively (Table S1). The bond angles also show deviations from the ideal 109.5° value, the most dramatic of which is the P1−Zn1−P1 bond angle at 95.92(3)°. Such a departure from perfect $T_d$ symmetry is a strong indication that the Zn−P bonding cannot be appropriately described by sp$^3$ hybridization, akin to $CH_4$. More information along these lines can be found in the discussion of the electronic structure (*vide infra*). Such distorted $ZnP_4$ tetrahedra are common structural fragments that are featured in a wide variety of structures.[13,47−49]

The Zn1-centered tetrahedra are edge-shared, through P1 atoms, with one another down the crystallographic *b*-axis, while they also are corner-shared, through P2 atoms, to adjacent Zn2-centered tetrahedra down both the crystallographic *a*- and *c*-axis. Finally, the Zn2 atoms, coordinated to four P atoms, are further connected to one another down the


https://doi.org/10.1021/acs.inorgchem.1c02209
Inorg. Chem. XXXX, XXX, XXX−XXX

*b*-axis through corner sharing, where the corners are P2 atoms. Such an interconnected network of $ZnP_4$ tetrahedra creates a polyanionic framework, $[Zn_2P_2]^{2-}$, that form cages around the divalent Ba atoms. These $Ba^{2+}$ cations perfectly balance the charge from the anionic cages, making $BaZn_2P_2$ a valence precise composition, adhering to the Zintl–Klemm formalism.[15,50]

Continuing, the sizable $Ba^{2+}$ cations are surrounded by a large number of anions. The cage-like motif made up of corner- and edge-shared $ZnP_4$ tetrahedra, as previously mentioned, where $Ba^{2+}$ are found, is depicted in Figure 1c.

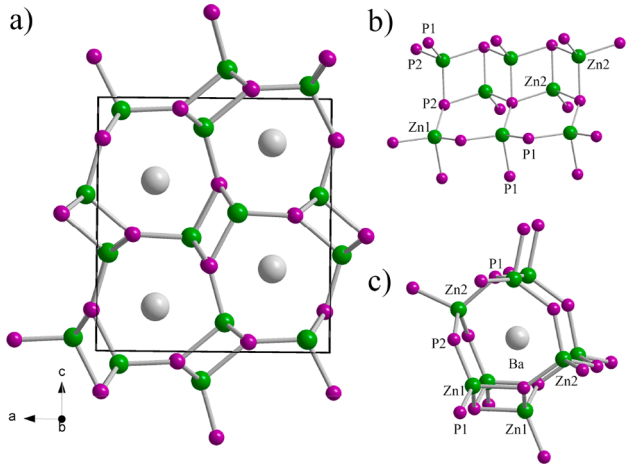


**Figure 1.** (a) Crystal structure of $\alpha$-$BaZn_2P_2$, viewed down the crystallographic *b*-axis. The Ba, Zn, and P atoms are represented as gray, green, and purple spheres, respectively. Unit cell is outlined. (b) Interconnection modes of the $ZnP_4$ tetrahedra. (c) Cage-like structure that the Zn and P atoms form around the divalent Ba cations.

Such an arrangement of atoms surrounding each $Ba^{2+}$ cation allows for it to be in proximity of seven P atoms at distances varying between 3.192(1) and 3.497(1) Å, and five Zn atoms, with distances varying between 3.2591(7) and 3.5972(6) Å. The Ba–P interatomic distances cited above, as one can notice, have a much wider range when compared to typical distances in structures of other ternary phosphides. For reference, $Ba_2ZnP_2$, the only other unrelated compound identified in the Ba–Zn–P ternary system, has Ba–P distances that vary from 3.317 to 3.466 Å.[49] Such a wide range of distances is not seen in compounds in the related Ba–Cd–P system either with $BaCd_2P_2$ having consistent distances (3.237–3.238 Å)[51] and $Ba_2CdP_2$ having Ba–P distances ranging from 3.114 to 3.345 Å.[52] Thus, the wide range of Ba–P distances seen for $\alpha$-$BaZn_2P_2$ could hint at thermal instabilities in the Ba positions.

**$\beta$-$BaZn_2P_2$.** Before we start the discussion of the crystal structure of the $\beta$-$BaZn_2P_2$ polymorph, we should note the difficulty of obtaining a suitable crystal of $\beta$-$BaZn_2P_2$ for single-crystal X-ray diffraction experiments. As it is well-known from prior research efforts synthesizing layered $BaMn_2Bi_2$[53] and $BaZn_2P_2$[23] compounds which crystallize in the $ThCr_2Si_2$ structure type, they are ductile and difficult to cut. Therefore, all manipulations of the crystals to be used for single-crystal X-ray diffraction experiments are difficult. Attempts to cut single crystal for the appropriate size usually result in the shape deformation, which concomitantly affect the quality of the single-crystal data. Smeared reflections are usually observed for such deformed crystals. However, data of suitable quality for structural work can be achieved through the measurement of an unaltered crystal of $\beta$-$BaZn_2P_2$ obtained directly after reaction.

The beta form of $BaZn_2P_2$ was first identified by Klüfers and Mewis in the late 1970s, alongside the As analogue of the alpha structure.[23] However, structures of $\beta$-$BaZn_2Pn_2$ (*Pn* = P, As) ternary phases lack precision single-crystal studies which is attributed to the above-mentioned reasons. With this work, we improve upon the structural knowledge with updated diffraction experiments, refined atomic coordinates, and revisited description of the crystal structure.

There are three unique atomic positions in the $\beta$-$BaZn_2P_2$ crystal structure, each occupied by a different atom. The Ba atoms adopt a 2*a* site (symmetry 4/*mmm*), while the Zn and P atoms are located at 4*d* and 4*e* Wyckoff sites (symmetry $\bar{4}m2$ and 4*mm*), respectively. This arrangement of atoms, as well as the crystallographic information, indicates that the compound crystallizes in the previously identified, and well-known, $ThCr_2Si_2$ structure type.[17] Because the crystal structure of compounds within the $ThCr_2Si_2$ structure type does not need an elaborate description, our presentation will be very brief.

The overall structure of $\beta$-$BaZn_2P_2$ can be seen in Figure 2a, as viewed down the crystallographic *a*-axis. The Zn atoms are

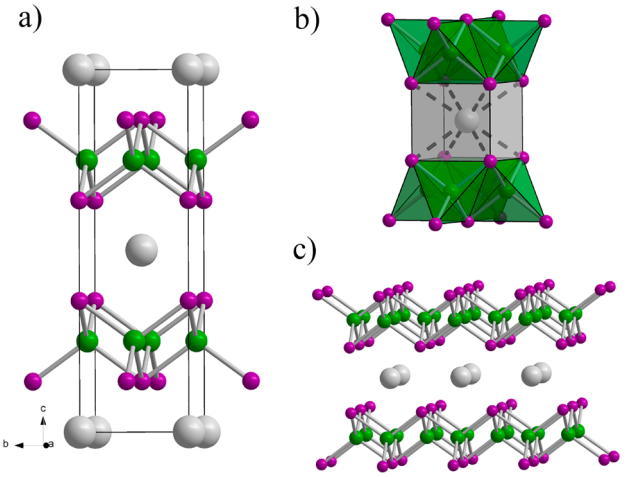


**Figure 2.** (a) Crystal structure of $\beta$-$BaZn_2P_2$, viewed down the crystallographic *a*-axis. The Ba, Zn, and P atoms are represented as gray, green, and purple spheres, respectively. Unit cell is outlined. (b) The simple cubic-like coordination of the $Ba^{2+}$ cations to adjacent $P^{3-}$ anions. (c) The $[Zn_2P_2]^{2-}$ layers that the Zn and P atoms form, separated by a layer of divalent Ba cations. The shortest interlayer distance is almost 3.7 Å long.

coordinated to four P atoms in the form of nearly ideal $ZnP_4$ tetrahedra. All Zn–P distances are the same (2.495(2) Å), and bond angles are, at most, less than 2° away from 109.5°. Here we note that the Zn–P distances featured in $\beta$-$BaZn_2P_2$ are in the middle of the range of distances seen for the $\alpha$-phase. Continuing, the tetrahedra are edge-shared with one another within the crystallographic *ab*-plane. These conjoining tetrahedra create polyanionic layers, $[Zn_2P_2]^{2-}$, which are stacked down the *c*-axis (Figure 2c), alternating with slabs of $Ba^{2+}$ cations. One should notice that there are no corner-to-corner P–P contacts along the *c*-axis (>3.65 Å), as known for the parental $BaAl_4$ structure type[54] where the eight Al atoms closest to the $Ba^{2+}$ cation participate in a fifth homonuclear bond down the *c*-axis. Such a connection in $BaAl_4$ creates a 3D, cage-like structure around each Ba cation, whereas the lack of these contacts in $\beta$-$BaZn_2P_2$ and related structures creates the


https://doi.org/10.1021/acs.inorgchem.1c02209
Inorg. Chem. XXXX, XXX, XXX–XXX

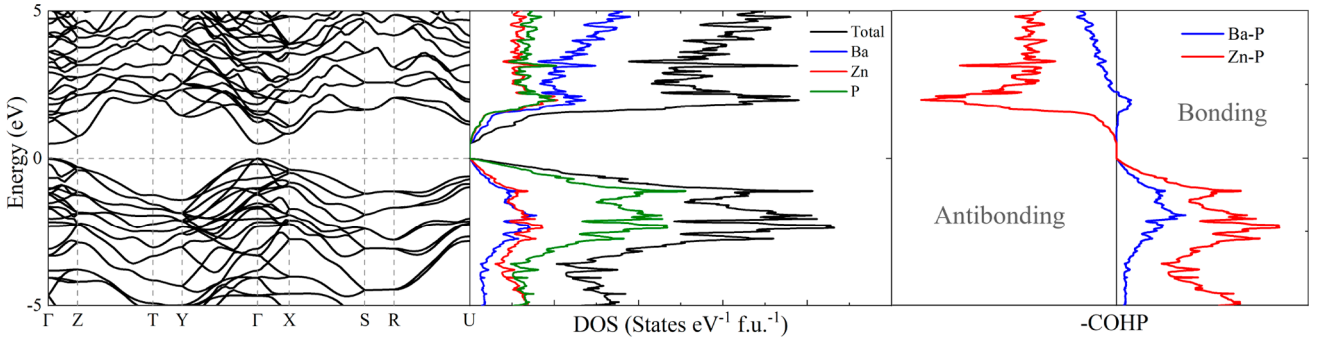


**Figure 3.** Electronic structure and bonding analysis for $\alpha$-$BaZn_2P_2$ represented in three panels. The calculated band structure is shown in the left panel (a closer look at the bands closest to the Fermi level is shown in Figure S6). The total and partial density of states (DOS) are shown in the center panel, and the Crystal Orbital Hamilton Population (COHP) curves for the Ba−P and Zn−P bonds are shown in the right panel.

above-mentioned 2D layered framework. While the 2D framework still allows for the $Ba^{2+}$ cations of $\beta$-$BaZn_2P_2$ to be in a nearly cubic arrangement with respect to P atoms (i.e., all Ba−P distances are equidistant (3.400(2) Å)), the subtle difference between these structures is with worth discussing. The inherent difference is the necessity to maintain charge balance in the $BaAl_4$ system with fewer electrons. The Al system is electron-poor when compared to $\beta$-$BaZn_2P_2$ ($14e^-$ vs $16e^-$, respectively) which forces the Al atoms closest to the cation to adopt a fifth bond as previously mentioned. This translates to the charge balance in the latter case being easily understood by using the Zintl concept ($(Ba^{2+})(Zn^{2+})_2(P^{3-})_2$), whereas the former case is nontrivial.[55] However, it can still be understood by using the Zintl concept through a simplification: if one considers the 4-coordinate Al atoms as strictly cations and the 5-coordinate Al atoms as strictly anions (like in $\beta$-$BaZn_2P_2$). If this simplification is made, then the charge balance is similarly reduced to $(Ba^{2+})(Al^{3+})_2(Al^{4-})_2$, making it easily understood why the fifth bond is required for charge balance in $BaAl_4$.

**Structural Phase Transition.** A potential phase transition ($\alpha \rightarrow \beta$) was first identified based on the thermogravimetric analysis (see Figure S5), as mentioned in the Experimental Section. Fluctuations in the heating portion of the calorimetry graph begin at ∼840 K and continue throughout the remainder of the heating mode. A strong thermal event during heating was identified at ca. 1146 K, but the cause of the said event is unknown. The thermogravimetry portion of the experiment indicated that the sample began to thermally decompose above that temperature. Such decomposition accounted for the loss of ∼10% of the original weight of the sample once the experiment was completed. Continuing, during the cooling portion of the experiment, another thermal event was identified at ca. 1025 K, which serves as evidence for a potential phase transition or recrystallization of the starting material. Based on these findings, further experiments were conducted, probing the high-temperature regime seen in the TG/DSC analysis.

Several experiments were conducted following the same general strategy described here. A synthesized sample (0.2−0.4 g) with the bulk containing primarily $\alpha$-$BaZn_2P_2$ (see Figure S1) was mechanically ground and cold pressed into a 1/4 in. pellet and then subsequently flame-sealed in a silica jacket. The pellet itself was first placed inside an alumina crucible with a bottom lined with inert Mo foil. This reactor vessel was then placed into a furnace for heat treatment.

First an above-mentioned prepared pellet was annealed at 1063 K for ∼3 days and subsequently quenched in cold water. The results of such an experiment proved that the thermal energy at 1063 K was not sufficient to contribute to the phase transition from the $\alpha$- to the $\beta$-$BaZn_2P_2$ structure—the results of the powder X-ray diffraction experiments before and after the annealing revealed no changes (Figure S3). Following this, the experiment was repeated with a higher annealing temperature of 1123 K (ca. 20 K below the noted thermal even; *vide supra*). Once again after an annealing step of ∼3 days, the reaction was quenched in water. This time the phase transition between the $\alpha$- and $\beta$-phase was confirmed by PXRD as the pattern before and after the heat treatment showed a transition from the orthorhombic "1−2−2" structure to the tetragonal modification, with small amounts of the $\alpha$-polymorph left (see Figure S3). Another pellet also with a bulk composition of $\alpha$-$BaZn_2P_2$ was then placed in the furnace and annealed following the same temperature profile, but the sample was instead cooled to 573 K at a rate of 10 K/h to investigate the issue of the reversibility of the first-order $\alpha \rightarrow \beta$ phase transition. After the annealing and cooling step, the diffraction pattern showed a mixture of both polymorphs, indicating the potential for the transition to be reversible when allowing the high-temperature phase to slowly cool (see Figure S4).

Further experimentation to access the potential reversibility of the phase transition involved the same process but taking a prepared bulk sample of the tetragonal $\beta$-phase instead (see Figure S2). Two reactions were prepared from this starting material, and the resulting pellets were annealed at the same temperature as stated previously (1123 K). One sample was quenched at the same high temperature while the other was slowly cooled to 573 K with a rate of 5 K/h.

However, when annealing a bulk sample of $\beta$-$BaZn_2P_2$ at the same temperature and allowing it to slowly cool, the sample remained in the $\beta$-$BaZn_2P_2$ structural form. Therefore, the reversibility of the phase change cannot be confirmed based on the current experimental evidence, but the presence of such a transition ($\alpha \rightarrow \beta$) is ultimately not surprising since the As analogue also demonstrates a proclivity for such a structural transition at high temperatures, as previously mentioned.[1] More research into the thermochemistry of $BaZn_2P_2$ is warranted to understand the subtleties of the transition. Quantifying the temperature points will be important should $BaZn_2P_2$ be pursued for thermoelectric properties optimizations.


https://doi.org/10.1021/acs.inorgchem.1c02209
Inorg. Chem. XXXX, XXX, XXX−XXX

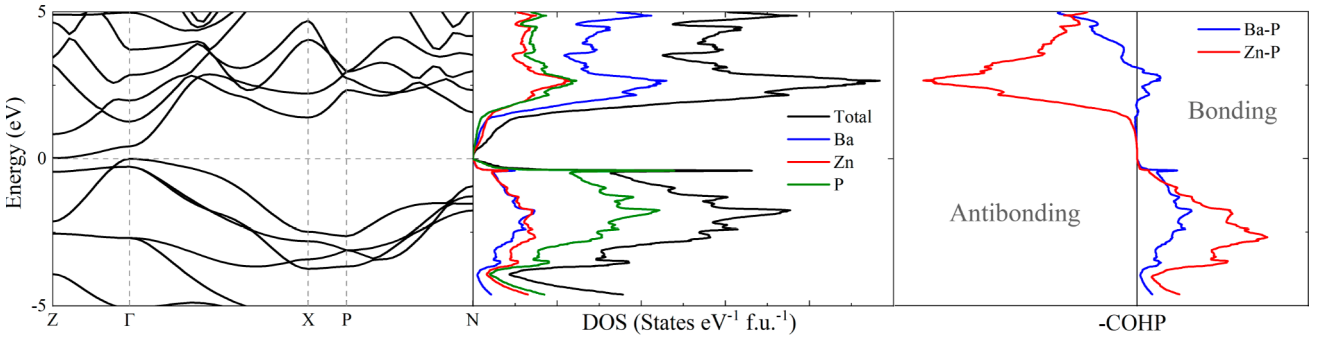


**Figure 4.** Electronic structure and bonding analysis for $\beta$-$BaZn_2P_2$ shown in three panels. The calculated band structure is shown in the left panel (a closer look at the bands closest to the Fermi level is shown in Figure S7). The total and partial density of states (DOS) are shown in the center panel, and the Crystal Orbital Hamilton Population (COHP) curves for the Ba−P and Zn−P bonds are shown in the right panel.

**Electronic Structure of $\alpha$-$BaZn_2P_2$.** The electronic structure of $\alpha$-$BaZn_2P_2$ was calculated to better understand the electronic transport and chemical bonding exhibited by the compound. The combined band structure plot, density of states, and Crystal Orbital Hamilton Population curves can be seen in Figure 3. As to be expected based on the understanding of the Zintl concept, $\alpha$-$BaZn_2P_2$ is a semiconducting material with a calculated direct bandgap of ∼0.5 eV. This direct gap is located at the Γ point in the Brillouin Zone, for which there are two of them. The gap is symmetric, with the value being the same across both points. The symmetry of the bandgap likely points to the band degeneracy, which can in turn promote the thermoelectric performance of this phase. Furthermore, the realization of a narrow and direct bandgap at the Γ symmetry points to the possibility of band inversion via anisotropic strain tuning that can result in a nontrivial topological insulating state.

Closest to the Fermi level, the valence band is dominated by contributions from the P atoms, specifically the P 3p-orbitals. These contributions extend below the Fermi level to approximately −3.6 eV. There are also some minor contributions from the Ba and Zn atoms within this window particularly the d- and p-orbitals for Ba and Zn, respectively. The former indicates mixing of the P p-orbitals and the Ba d-orbitals, which hints at some degree of covalency between P and Ba. Such a phenomenon is a subtle departure from the Zintl−Klemm concept which considers Ba as exclusively an electron donor. The overlapping of the P and Zn orbitals strongly indicates covalent bonding between the two atoms. Their states continue to overlap further below the Fermi level (−3.6 to −5 eV) where the Zn s-orbitals contribute more to the states alongside the P p-orbitals. The clear separation of the Zn s- and p-orbitals, however, indicates that even though they are the frontier orbitals involved in Zn−P bonding, they are not $sp^3$ hybridized, as noted earlier. This deviation would help to explain the structural distortions of the $ZnP_4$ tetrahedra away from the ideal $T_d$ symmetry. The conduction band nearest the Fermi level is composed of contributions from all three atoms, specifically the P p-orbitals, the Zn s-orbitals, and the Ba d-orbitals. However, the more significant contribution originates from the Ba d-orbitals. It is noted that the magnitude of the total density of state here is about 4 times higher than that of $\beta$-$BaZn_2P_2$ (*vide infra*) which is a likely indication of a more enhanced magnitude of Seebeck coefficient for this phase.

The Crystal Orbital Hamilton Population curves are presented for $\alpha$-$BaZn_2P_2$ for Ba−P and Zn−P pairs in Figure 3. The average Ba−P and Zn−P bonds are in the bonding state below the Fermi level, indicating that the interactions are optimized. There is a strong antibonding nature about the Zn−P bonds above the Fermi level, while there are some bonding states for the Ba−P interactions within energy window from ca. 1.0 to 2.2 eV. Such bonding states perhaps indicate the potential for electron doping on the Ba sites within the structure.

**Electronic Structure of $\beta$-$BaZn_2P_2$.** The electronic band structure, total and partial density of states (DOS), and Crystal Orbital Hamilton Populations (COHP) curves (Figure 4) were calculated to gain a better understanding of the nature of the chemical bonding featured in $\beta$-$BaZn_2P_2$. As seen from the band structure and DOS plots, the compound is a small bandgap semiconductor with an indirect bandgap of ∼0.03 eV. Note that this theoretically calculated gap is smaller than the experimentally determined bandgap of $\beta$-$BaZn_2As_2$, which was stated to be 0.23 eV by Xiao et al.[56]

This goes against the traditional idea that the gap should be larger for the phosphide since P is more electronegative and thus the bonds are more ionic in character. However, such a discrepancy is not surprising since it is a known fact that muffin-tin approximation that is implemented in the LMTO-ASA code is not well suited for compounds that have a covalently bonded layered framework.[57] In fact, when the same methodology is used to calculate the electronic structure of $\beta$-$BaZn_2As_2$ based on its atomic coordinates and unit cell parameters, the resulting density of states shows a closing of the bandgap to a pseudogap. Therefore, we can predict that the experimentally measured bandgap for $\beta$-$BaZn_2P_2$ would be greater, probably exceeding the 0.23 eV value for $\beta$-$BaZn_2As_2$.[56] This speculation could not be reconciled with experimental data as a part of this study since large enough single crystals of $\beta$-$BaZn_2P_2$ (or phase-pure polycrystalline material) were not available. It is important to note that the nature of the band structure of the $\beta$-$BaZn_2P_2$ phase would likely lead to a trivial insulating state, although in-depth studies are required to establish the nature of the topological properties of this phase. This, however, does not rule out the likely realization of enhanced thermoelectric properties of this material with proper band engineering.

The valence band nearest to the Fermi level is predominantly composed of contributions from P, more specifically the frontier p-orbitals. There are some minor contributions, though, from the Zn- and Ba-originated state further below the Fermi level (0 to −3.7 eV), where the region is still dominated the P 3p-orbitals. The Ba states within this region are primarily


https://doi.org/10.1021/acs.inorgchem.1c02209
Inorg. Chem. XXXX, XXX, XXX−XXX

made up of the d-orbitals, and the Zn states within the same region are composed of the Zn p-orbitals. The former is more surprising than the latter since the p−d mixing, once again, implies a character of covalency between Ba and P, and the latter is what would be expected for the electronic states of a Zn−P bond. Interestingly, the Zn and P DOS continue to overlap further down (−3.7 to −5.6 eV)

Just above the Fermi level nearest the conduction band minimum (CBM), all three atoms contribute to the states with the most significant being from the Zn s-orbitals. Further above the CMB (1.4−5 eV) the Ba d-orbitals are the primary contributor to the states with contributions from both the P p-orbitals and the Zn s- and p-orbitals. The Zn s- and p-orbitals are separated, though, with the s-orbitals contributing most in within the region closer to the CBM (0−3.4 eV) and p-orbitals taking over following the crossover point at 3.4 eV.

The Crystal Orbital Hamilton Population curves for Ba−P and Zn−P interactions are also presented in Figure 4. The Ba−P and Zn−P bonds are fully optimized with both of them being in the bonding state below the Fermi level. Above the Fermi level, though, there are some bonding states within the Ba−P interactions within the regions 1.4−1.7 and 2−3 eV.

**Thermopower and Transport Properties of α-$BaZn_2P_2$.** The temperature dependence of electrical resistivity $\rho(T)$ of the α-$BaZn_2P_2$ phase in the temperature range 300−400 K is presented in Figure 5a. $\rho(T)$ achieves about 38.7 mΩ·cm at 400 K, which falls in the range of values observed for similar semiconducting materials. The assertion of a semiconducting behavior in this phase is further confirmed by a gradual increase in $\rho(T)$ upon cooling to room temperature where it attains a value of ca. 46 mΩ·cm. The $\rho(T)$ properties presented here are consistent with the depiction of both the electronic band structure and density of state shown in Figure 3, where a narrow bandgap $E_g \sim 0.5$ is observed as well as the Zintl concept of closed-shell configuration. It is worth noting that considering the general feature of the $\rho(T)$ curve, one would expect a further drop in its magnitude for temperatures above 400 K (being the highest temperature we were able to measure). This observation and the steeply increasing nature and magnitude of Seebeck coefficient $S(T)$ (*vide infra*) would prove invaluable for enhancing the thermoelectric figure of merit in this phase.

Figure 5b presents the temperature variation of Seebeck coefficient $S(T)$ in the temperature range 300−620 K. The black and red spheres represent two separate heating measurements. The observed magnitude of $S(T)$ at room temperature (black spheres) is 143.5 μV/K. This value is remarkably high for as-synthesized sample, and it is comparable to observations in several excellent thermoelectric materials such as $Sr_5Al_2Sb_6$[58] and $CaZn_2Sb_2$.[59] Upon further heating, $S(T)$ achieved an even more significant value of ca. 190 μV/K at 600 K. Judging from the shape of the curve, the material could achieve higher values at elevated temperatures. A second measurement (red spheres) on a different crystal reveals a slight drop in the magnitude of $S(T)$, although with similar power-law behavior. This difference in magnitude of the Seebeck coefficient may be attributed mainly to slight differences in geometric factors between the two samples used for such measurements. It is, however, noted that the observed magnitudes of the Seebeck coefficients in both samples are comparable and of the same order of magnitude. Here the magnitude of $S(T)$ varies from 180.2 to 119 μV/K between 620 and 300 K. An important observation in $S(T)$ is its positive slope throughout the temperature range studied and indicates the significant role of holes in producing the thermal voltage difference across the ends of this material, where the electrons are the minority charge carriers. Hence, α-$BaZn_2P_2$ would fit into the description of an intrinsic p-type semiconductor. Furthermore, the p-type semiconducting behavior provides even stronger support for the position of the Fermi energy, as seen in Figure 3. Because the holes are the dominant carriers, this would normally imply that more holes would be found at the valence band than the number of electrons in the conduction band; thus, there is a more likelihood of finding a hole at the valence band than finding an electron at the conduction band. Hence, the Fermi level is expected to be much closer to the valence band, which is the picture conveyed by Figure 3. Perhaps the same picture would hold too for β-$BaZn_2P_2$ presented in Figure 4, although the transport properties are not yet available.

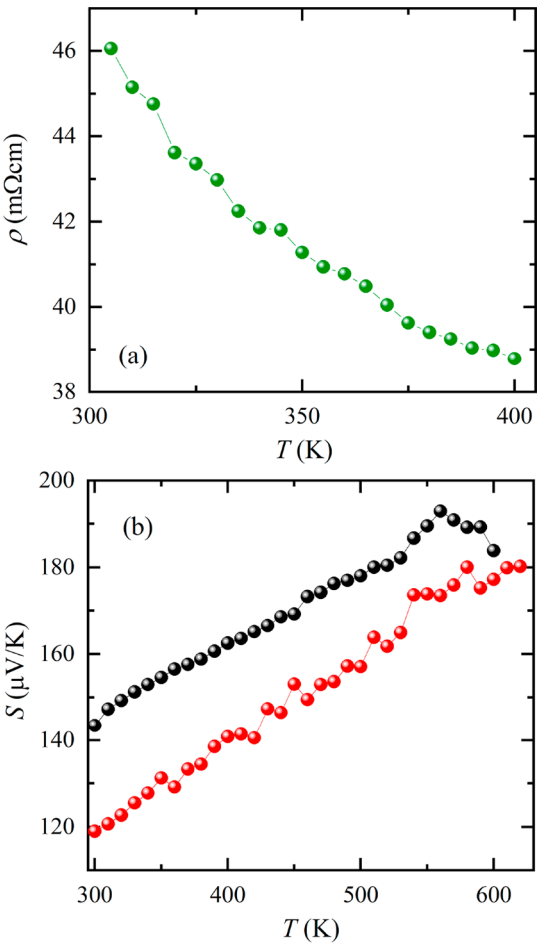


**Figure 5.** (a) $\rho(T)$ of single-crystalline α-$BaZn_2P_2$ phase. (b) $S(T)$ of single-crystalline α-$BaZn_2P_2$ phase for two different heating mode experiments.

In addition, the experimental bandgap may be estimated from the $S(T)$ result based on the expression $E_g = 2e|S_{max}|T_{max}$, where $E_g$ is the bandgap, $e$ is the electron charge, and $S_{max}$ is the maximum value of $S$ observed at a maximum temperature $T_{max}$ considered. Taking the values of $S_{max} = 190$ μV/K at $T_{max} = 600$ K yields $E_g = 0.23$ eV. We state here that although this analysis is useful for getting an experimental estimation of the bandgap of the material, the values used for $T_{max}$ and $S_{max}$ may not be the true values as $S(T)$ will likely continue to increase


https://doi.org/10.1021/acs.inorgchem.1c02209
Inorg. Chem. XXXX, XXX, XXX−XXX

within the temperature regime beyond what was measured in this study. This estimation although is half the theoretical value observed from our band structure calculations and is comparable to the experimental value[1,54] in $BaZn_2As_2$. The deviation of the experimental value from the theoretical prediction may be associated with the likely overestimation of $E_g$ in this present case. However, it would be plausible to project that a reconcilable value with the theoretical value may be achieved at temperatures above 600 K as stated previously.

With the increasing interest in investigating the electrical and thermal transport properties of several "1−2−2" phases for promising thermoelectric and topological properties,[60] we posit that the $\alpha$-$BaZn_2P_2$ phase holds the potential of being an excellent candidate for exploring these properties because of the magnitude and temperature dependence of $S(T)$ at elevated temperatures as well as its cage-like crystal structure. The crystal structure wherein the Ba atom is situated in an oversized cage-like structure formed by Zn and P atoms presents an opportunity for the rattling effect, significantly suppressing the lattice thermal conductivity of this material. Although the thermal conductivity of this phase is not immediately available, the trends in the various "1−2−2" phases are in strong support of a reasonably low thermal conductivity, which may even be further suppressed in this phase due to the possibility of rattling effect produced by the Ba atom. It is also not unusual to expect that the effect of likely lattice instability that may be resident in this structure as a result of its metastable nature would also play key roles in suppressing its thermal conductivity as found in $Ba_{1-x}K_xZn_2As_2$.[1] At the present, a drawback to the thermoelectric properties of this phase is the magnitude of measured $\rho(T)$ with values that are nearly an order of magnitude higher than other materials in the same class,[61,62] thereby placing a limit on the thermoelectric power factor (PF = $S^2/\rho$) that can be estimated at 400 K to be ca. 0.07 mW/(m $K^2$), which is a factor of ∼3 lower than the As analogue at the same temperature.[32] The origin of such an enhanced $\rho(T)$ is not immediately clear, and the fact that data have not been collected for temperatures above 400 K warrants a revisit at the electrical transport of this phase so as to properly conceptualize its thermoelectric properties. Such a follow-up investigation would also benefit from optimizing the charge carrier concentration and mobility through appropriate doping.

Lastly, we comment on the $\beta$-$BaZn_2P_2$ phase with the layered structure. Although, this phase's physical properties are not available at present, one can draw relevant parallels from the reports on the $BaZn_2Sb_2$ phase—a relatively low thermal conductivity 1.6 W/(m K) and $zT$ = 0.36 at 675 K have been reported[33] for the latter, which could serve as a useful clue to some interesting properties that reside in $\beta$-$BaZn_2P_2$. The layered crystal structure of this phase is of particular importance since these structural motifs have been found to promote the realization of low thermal conductivity, whereby phonon anharmonicity brings about interactions between the alternating layers.

## CONCLUSION

Two "1−2−2" Zintl phases, which are polymorphs, were synthesized and characterized—the orthorhombic $\alpha$-$BaZn_2P_2$ modification being synthesized for the first time and the $\beta$-$BaZn_2P_2$ tetragonal phase being resynthesized. The former $\alpha$-$BaZn_2P_2$ adopts the $\alpha$-$BaCu_2S_2$ structure type while the latter crystallizes in the well-explored and studied $ThCr_2Si_2$ type. Like some of the other compounds within the $\alpha$-$BaCu_2S_2$ structure type, $\alpha$-$BaZn_2P_2$ exhibits a high-temperature phase transition to the $\beta$-phase after being annealed in a furnace at 1123 K for several days. At a first glance, such a transition closes the door for the use of $\alpha$-$BaZn_2P_2$ in high-temperature thermoelectric applications since such a phase transition will disrupt the desired properties in these high-temperature regimes. However, an example of $Ba_{1-x}K_xZn_2As_2$ shows that the metastable nature of this phase is indeed to a better advantage of realizing excellent performance.[12] The calculated electronic structures of both compounds show that they are both small gap semiconductors with a calculated bandgap of $E_g$ = 0.5 and 0.03 eV for $\alpha$- and $\beta$-$BaZn_2P_2$, respectively. Preliminary transport property measurements for $\alpha$-$BaZn_2P_2$ point to the compound being a p-type semiconductor with the Seebeck coefficient achieving a value of 184 $\mu$V/K at 600 K. The electrical resistivity of the compound, though, decreases with increasing temperature and has a higher overall magnitude than typical semimetal materials. While the identified phase transition and preliminary measurements are interesting and exciting findings, more research is warranted in the areas of deciphering the potential reversibility of the phase transition as well as tuning the physical properties to extract a higher thermoelectric potential ($zT$). It is expected that the cage-like motif of the $\alpha$-phase and the layers in the $\beta$-structure will allow for a low thermal conductivity to be realized. This combined with the apparent air stability makes these materials promising for further thermoelectric applications.

## ASSOCIATED CONTENT

### Supporting Information

The Supporting Information is available free of charge at https://pubs.acs.org/doi/10.1021/acs.inorgchem.1c02209.

Table S1: interatomic distances; Figures S1−S7: results from powder diffraction experiments, thermal analysis, and electronic structure calculations (PDF)

### Accession Codes

CCDC 2096557−2096558 contain the supplementary crystallographic data for this paper. These data can be obtained free of charge via www.ccdc.cam.ac.uk/data_request/cif, or by emailing data_request@ccdc.cam.ac.uk, or by contacting The Cambridge Crystallographic Data Centre, 12 Union Road, Cambridge CB2 1EZ, UK; fax: +44 1223 336033.

## AUTHOR INFORMATION


### Corresponding Author

**Svilen Bobev** − *Department of Chemistry and Biochemistry, University of Delaware, Newark, Delaware 19716, United States;* orcid.org/0000-0002-0780-4787; Email: bobev@udel.edu

### Authors

**Adam Balvanz** − *Department of Chemistry and Biochemistry, University of Delaware, Newark, Delaware 19716, United States*

**Sviatoslav Baranets** − *Department of Chemistry and Biochemistry, University of Delaware, Newark, Delaware 19716, United States;* orcid.org/0000-0003-3449-3344

**Michael O. Ogunbunmi** − *Department of Chemistry and Biochemistry, University of Delaware, Newark, Delaware 19716, United States*

Complete contact information is available at:




https://doi.org/10.1021/acs.inorgchem.1c02209
Inorg. Chem. XXXX, XXX, XXX−XXX

https://pubs.acs.org/10.1021/acs.inorgchem.1c02209

## Notes

The authors declare no competing financial interest.

## ■ ACKNOWLEDGMENTS

This work was financially supported by the US Department of Energy through Grant DE-SC0008885. The undergraduate research program at the University of Delaware is also acknowledged for providing A.B. the opportunity to complete this research. The authors express gratitude to Dr. Julien Makongo for preliminary work in the Ba−Zn−P system.

## ■ REFERENCES

(1) Kunioka, H.; Kihou, K.; Kato, D.; Usui, H.; Iida, T.; Nishiate, H.; Kuroki, K.; Yamamoto, A.; Lee, C.-H. Thermoelectric Properties of (Ba,K)$Zn_2As_2$ Crystallized in the $ThCr_2Si_2$-Type Structure. *Inorg. Chem.* **2020**, *59* (9), 5828−5834.

(2) Dolyniuk, J.-A.; Wang, J.; Marple, M. A. T.; Sen, S.; Cheng, Y.; Ramirez-Cuesta, A. J.; Kovnir, K. Chemical Bonding and Transport Properties in Clathrates-I with Cu-Zn-P Frameworks. *Chem. Mater.* **2018**, *30* (10), 3419−3428.

(3) Zevalkink, A.; Zeier, W. G.; Cheng, E.; Snyder, J.; Fleurial, J.-P.; Bux, S. Nonstoichiometry in the Zintl Phase $Yb_{1-\delta}Zn_2Sb_2$ as a Route to Thermoelectric Optimization. *Chem. Mater.* **2014**, *26* (19), 5710−5717.

(4) Takagiwa, Y.; Sato, Y.; Zevalkink, A.; Kanazawa, I.; Kimura, K.; Isoda, Y.; Shinohara, Y. Thermoelectric Properties of $EuZn_2Sb_2$ Zintl Compounds: ZT Enhancement through Yb Substitution for Eu. *J. Alloys Compd.* **2017**, *703*, 73−79.

(5) Chen, C.; Xue, W.; Li, S.; Zhang, Z.; Li, X.; Wang, X.; Liu, Y.; Sui, J.; Liu, X.; Cao, F.; Ren, Z.; Chu, C. W.; Wang, Y.; Zhang, Q. Zintl-Phase $Eu_2ZnSb_2$: A Promising Thermoelectric Material with Ultralow Thermal Conductivity. *Proc. Natl. Acad. Sci. U. S. A.* **2019**, *116* (8), 2831−2836.

(6) Baranets, S.; Ovchinnikov, A.; Bobev, S. Structrual Diversity of Zintl Phictides with Rare-Earth Metals. In *Handbook on the Physics and Chemistry of Rare Earths*: 2021, in press.

(7) Stoyko, S. S.; Khatun, M.; Mar, A. Ternary Arsenides $A_2Zn_2As_3$ ($A$ = Sr, Eu) and Their Stuffed Derivatives $A_2Ag_2ZnAs_3$. *Inorg. Chem.* **2012**, *51* (4), 2621−2628.

(8) Baranets, S.; Bobev, S. From the Ternary Phase $Ca_{14}Zn_{1+\delta}Sb_{11}$ ($\delta \asymp 0.4$) to the Quaternary Solid Solutions $Ca_{14-x}RE_xZnSb_{11}$ ($RE$ = La-Nd, Sm, Gd, $x \asymp 0.9$). A Tale of Electron Doping via Rare-Earth metal Substitutions and the Concomitant Structural Transformations. *Inorg. Chem.* **2019**, *58* (13), 8506−8516.

(9) Liu, X. C.; Wu, Z.; Xia, S. Q.; Tao, X. T.; Bobev, S. Structural Variability versus Structural Flexibility. A Case Study of $Eu_9Cd_{4+x}Sb_9$ and $Ca_9Mn_{4+x}Sb_9$ ($x \approx 1/2$). *Inorg. Chem.* **2015**, *54* (3), 947−955.

(10) Baranets, S.; Darone, G. M.; Bobev, S. Synthesis and Structure of $Sr_{14}Zn_{1+x}As_{11}$ and $Eu_{14}Zn_{1+x}As_{11}$ ($x \leq 0.5$). New Members of the Family of Pnictides Isotypic with $Ca_{14}AlSb_{11}$, Exhibiting a New Type of Structrual Disorder. *J. Solid State Chem.* **2019**, *280*, 120990.

(11) Suen, N. T.; Wang, Y.; Bobev, S. Synthesis, Crystal Structures, and Physical Properties of the New Zintl Phases $A_{21}Zn_4Pn_{18}$ ($A$ = Ca, Eu; $Pn$ = As, Sb) - Versatile Arrangements of [Zn$Pn_4$] Tetrahedra. *J. Solid State Chem.* **2015**, *227*, 204−211.

(12) Wang, J.; Xia, S. Q.; Tao, X. T. Syntheses, Crystal Structure and Physical Properties of New Zintl Phases $Ba_3T_2As_4$ ($T$ = Zn, Cd). *J. Solid State Chem.* **2013**, *198*, 6−9.

(13) Wang, J.; Xia, S.-Q.; Tao, X.-T.; Schäfer, M. C.; Bobev, S. New Ternary Phosphides and Arsenides. Syntheses, Crystal Structures, Physical Properties of $Eu_2ZnP_2$, $Eu_2Zn_2P_3$ and $Eu_2Cd_2As_3$. *J. Solid State Chem.* **2013**, *205*, 116−125.

(14) Wilson, D. K.; Saparov, B.; Bobev, S. Synthesis, Crystal Structures and Properties of the Zintl Phases $Sr_2ZnP_2$, $Sr_2ZnAs_2$, $A_2ZnSb_2$ and $A_2ZnBi_2$ ($A$ = Sr and Eu). *Z. Anorg. Allg. Chem.* **2011**, *637* (13), 2018−2025.

(15) Ovchinnikov, A.; Bobev, S. Zintl Phases with Group 15 Elements and the Transition Metals: A Brief Overview of Pnictides with Diverse and Complex Structures. *J. Solid State Chem.* **2019**, *270* (22), 346−359.

(16) Schellenberg, I.; Eul, M.; Hermes, W.; Pöttgen, R. A $^{121}$Sb and $^{151}$Eu Mössbauer Spectroscopic Investigation of $EuMn_2Sb_2$, $EuZn_2Sb_2$, $YbMn_2Sb_2$, and $YbZn_2Sb_2$. *Z. Anorg. Allg. Chem.* **2010**, *636* (1), 85−93.

(17) Shatruk, M. $ThCr_2Si_2$ Structure Type: The "Perovskite" of Intermetallics. *J. Solid State Chem.* **2019**, *272*, 198−209.

(18) Peng, W.; Chanakian, S.; Zevalkink, A. Crystal Chemistry and Thermoelectric Transport of Layered $AM_2X_2$ Compounds. *Inorg. Chem. Front.* **2018**, *5*, 1744−1759.

(19) Toberer, E. S.; May, A. F.; Melot, B. C.; Flage-Larsen, E.; Snyder, G. J. Electronic Structure and Transport in Thermoelectric Compounds $AZn_2Sb_2$ ($A$ = Sr, Ca, Yb, Eu). *Dalton Trans.* **2010**, *39* (4), 1046−1054.

(20) Zhang, H.; Baitinger, M.; Tang, M. B.; Man, Z. Y.; Chen, H. H.; Yang, X. X.; Liu, Y.; Chen, L.; Grin, Y.; Zhao, J. T. Thermoelectric Properties of $Eu(Zn_{1-x}Cd_x)_2Sb_2$. *Dalton Trans.* **2010**, *39* (4), 1101−1104.

(21) Hlukhyy, V.; Trots, D.; Fässler, T. F. First-Order Phase Transition in $BaNi_2Ge_2$ and the Influence of the Valence Electron Count on Distortion of the $ThCr_2Si_2$ Structure Type. *Inorg. Chem.* **2017**, *56* (3), 1173−1185.

(22) Iglesias, J. E.; Pachali, K. E.; Steinfink, H. Structural Chemistry of $Ba_2CdS_3$, $Ba_2CdSe_3$, $BaCdS_2$, $BaCu_2S_2$ and $BaCu_2Se_2$. *J. Solid State Chem.* **1974**, *9* (1), 6−14.

(23) Klüfers, P.; Mewis, A. Zur Struktur Der Verbindungen $BaZn_2P_2$ Und $BaZn_2As_2$. *Z. Naturforsch., B: J. Chem. Sci.* **1978**, *33* (2), 151−155.

(24) Brechtel, E.; Cordier, G.; Schäfer, H. Darstellung Und Kristallstruktur von $BaMn_2Sb_2$, $BaZn_2Sb_2$ Und $BaCd_2Sb_2$. *Z. Naturforsch., B: J. Chem. Sci.* **1979**, *34* (7), 921−925.

(25) Huhnt, C.; Schlabitz, W.; Wurth, A.; Mewis, A.; Reehuis, M. First- and Second-Order Phase Transitions in Ternary Europium Phosphides with $ThCr_2Si_2$-Type Structure. *Phys. B* **1998**, *252* (1−2), 44−54.

(26) Mittal, R.; Mishra, S. K.; Chaplot, S. L.; Ovsyannikov, S. V.; Greenberg, E.; Trots, D. M.; Dubrovinsky, L.; Su, Y.; Brueckel, T.; Matsuishi, S.; Hosono, H.; Garbarino, G. Ambient- and Low-Temperature Synchrotron x-Ray Diffraction Study of $BaFe_2As_2$ and $CaFe_2As_2$ at Hihg Pressures up to 56 GPa. *Phys. Rev. B: Condens. Matter Mater. Phys.* **2011**, *83* (5), 054503.

(27) Uhoya, W.; Tsoi, G.; Vohra, Y. K.; McGuire, M. A.; Sefat, A. S.; Sales, B. C.; Mandrus, D.; Weir, S. T. Anomalous Compressibility Effects and Superconductivity of $EuFe_2As_2$ under High Pressures. *J. Phys.: Condens. Matter* **2010**, *22* (29), 292202.

(28) Huhnt, C.; Schlabitz, W.; Wurth, A.; Mewis, A.; Reehuis, M. First-Order Phase Transitions in $EuCo_2P_2$ and $SrNi_2P_2$. *Phys. Rev. B: Condens. Matter Mater. Phys.* **1997**, *56* (21), 13796−13804.

(29) Huhnt, C.; Michels, G.; Roepke, M.; Schlabitz, W.; Wurth, A.; Johrendt, D.; Mewis, A. First-Order Phase Transitions in the $ThCr_2Si_2$-Type Phosphides $ARh_2P_2$ ($A$ = Sr, Eu). *Phys. B* **1997**, *240* (1−2), 26−37.

(30) Huster, J.; Bronger, W. $\alpha$- Und $\beta$-$BaCu_2X_2$ ($X$ = S, Se) - Darstellung von Einkristallen in Kaliumchalkogenocyanat-Schmelzen. *Z. Anorg. Allg. Chem.* **1999**, *625* (12), 2033−2040.

(31) Leoni, S.; Carrillo-Cabrera, W.; Schnelle, W.; Grin, Y. $BaAl_2Ge_2$: Synthesis, Crystal Structure, Magnetic and Electronic Properties, Chemical Bonding, and Atomistic Model of the $\alpha \rightarrow \beta$ Phase Transition. *Solid State Sci.* **2003**, *5* (1), 139−148.

(32) Kihou, K.; Nishiate, H.; Yamamoto, A.; Lee, C.-H. Thermoelectric Properties of As-Based Zintl Compounds $Ba_{1-x}K_xZn_2As_2$. *Inorg. Chem.* **2017**, *56* (6), 3709−3712.



https://doi.org/10.1021/acs.inorgchem.1c02209
Inorg. Chem. XXXX, XXX, XXX−XXX

(33) Wang, X.-J.; Tang, M.-B.; Zhao, J.-T.; Chen, H.-H.; Yang, X.-X. Thermoelectric Properties and Electronic Structure of Zintl Compound $BaZn_2Sb_2$. *Appl. Phys. Lett.* **2007**, *90* (23), 232107.
(34) Yan, R.; Lv, W.; Wang, K.; Guo, K.; Yang, X.; Luo, J.; Zhao, J. T. Enhanced Thermoelectric Properties of $BaZn_2Sb_2$: Via a Synergistic Optimization Strategy Using Co-Doped Na and Sr. *J. Mater. Chem. A* **2016**, *4* (31), 12119−12125.
(35) Ryu, H.; Park, S. Y.; Li, L.; Ren, W.; Neaton, J. B.; Petrovic, C.; Hwang, C.; Mo, S.-K. Anisotropic Dirac Fermions in $BaMnBi_2$ and $BaZnBi_2$. *Sci. Rep.* **2018**, *8* (1), 15322.
(36) Balvanz, A.; Baranets, S.; Bobev, S. Synthesis and Structural Characterization of the New Zintl Phases $Ba_3Cd_2P_4$ and $Ba_2Cd_2P_3$. Rare Example of Small Gap Semiconducting Behavior with Negative Thermopower within the Range 300 K-700 K. *J. Solid State Chem.* **2020**, *289*, 121476.
(37) Bruker AXS Inc, *SAINT*, 2014.
(38) Bruker AXS Inc., *SADABS*, 2014.
(39) Sheldrick, G. M. SHELXT - Integrated Space-Group and Crystal-Structure Determination. *Acta Crystallogr., Sect. A: Found. Adv.* **2015**, *71* (1), 3−8.
(40) Dolomanov, O. V.; Bourhis, L. J.; Gildea, R. J.; Howard, J. A. K.; Puschmann, H. OLEX2: A Complete Structure Solution, Refinement and Analysis Program. *J. Appl. Crystallogr.* **2009**, *42* (2), 339−341.
(41) Sheldrick, G. M. Crystal Structure Refinement with SHELXL. *Acta Crystallogr., Sect. C: Struct. Chem.* **2015**, *71* (1), 3−8.
(42) Jepson, O.; Aderson, O. K. The STUTTGART TB-LMTO-ASA program;https://www2.fkf.mpg.de/andersen/LMTODOC/LMTODOC.html (accessed 2020-03-26).
(43) von Barth, U.; Hedin, L. A Local Exchange-Correlation Potential for the Spin Polarized Case. I. *J. Phys. C: Solid State Phys.* **1972**, *5* (13), 1629−1642.
(44) Steinberg, S.; Dronskowski, R. The Crystal Orbital Hamilton Population (COHP) Method as a Tool to Visualize and Analyze Chemical Bonding in Intermetallic Compounds. *Crystals* **2018**, *8* (5), 225.
(45) Wang, Y. C.; DiSalvo, F. J. Structure and Physical Properties of $BaCu_2Te_2$. *J. Solid State Chem.* **2001**, *156* (1), 44−50.
(46) Condron, C. L.; Hope, H.; Piccoli, P. M. B.; Schultz, A. J.; Kauzlarich, S. M. Synthesis, Structure, and Properties of $BaAl_2Si_2$. *Inorg. Chem.* **2007**, *46* (11), 4523−4529.
(47) Wang, J.; Lee, K.; Kovnir, K. Synthesis, Crystal Structure, and Properties of $La_4Zn_7P_{10}$ and $La_4Mg_{1.5}Zn_{8.5}P_{12}$. *Inorg. Chem.* **2017**, *56* (2), 783−790.
(48) Wang, J.; Yox, P.; Voyles, J.; Kovnir, K. Synthesis, Crystal Structure, and Properties of Three La-Zn-P Compounds with Different Dimensionalities of the Zn-P Framework. *Cryst. Growth Des.* **2018**, *18* (7), 4076−4083.
(49) Balvanz, A.; Baranets, S.; Bobev, S. Synthesis, Structural Characterization, and Electronic Structure of the Novel Zintl Phase $Ba_2ZnP_2$. *Acta Crystallogr., Sect. C: Struct. Chem.* **2020**, *C76*, 869−873.
(50) Nesper, R. The Zintl-Klemm Concept-A Historical Survey. *Z. Anorg. Allg. Chem.* **2014**, *640* (14), 2639−2648.
(51) Klüfers, P.; Mewis, A. $AB_2X_2$- Verbindungen Mit $CaAl_2Si_2$-Struktur. *Z. Kristallogr. - Cryst. Mater.* **1984**, *169* (1−4), 135−148.
(52) Balvanz, A.; Qu, J.; Baranets, S.; Ertekin, E.; Gorai, P.; Bobev, S. New *n*-Type Zintl Phases for Thermoelectrics: Discovery, Structural Characterization, and Band Engineering of the Compounds $A_2CdP_2$ ($A$ = Sr, Ba, Eu). *Chem. Mater.* **2020**, *32*, 10697.
(53) Saparov, B.; Sefat, A. S. Crystals, Magnetic and Electronic Properties of a New $ThCr_2Si_2$-Type $BaMn_2Bi_2$ and K-Doped Compositions. *J. Solid State Chem.* **2013**, *204*, 32−39.
(54) Pearson, W. B. the Most Populous of All Crystal Structure Types—the Tetragonal $BaAl_4$ Structure. *J. Solid State Chem.* **1985**, *56* (3), 278−287.
(55) Zheng, C.; Hoffmann, R. An Unusual Electron Count and Electron-Deficient Multi-Center Bonding in One Class of Intermetallics: The $BaAl_4$, $CaAl_2Zn_2$, $CeMg_2Si_2$ and FCC Al Structures. *Z. Naturforsch., B: J. Chem. Sci.* **1986**, *41* (3), 292−320.
(56) Xiao, Z.; Hiramatsu, H.; Ueda, S.; Toda, Y.; Ran, F. Y.; Guo, J.; Lei, H.; Matsuishi, S.; Hosono, H.; Kamiya, T. Narrow Bandgap in $\beta$-$BaZn_2As_2$ and Its Chemical Origins. *J. Am. Chem. Soc.* **2014**, *136* (42), 14959−14965.
(57) Reshak, A. H. Electronic Structure and Transport Properties of $Ba_2Cd_2Pn_3$ ($Pn$ = As and Sb): An Efficient Materials for Energy Conversion. *J. Alloys Compd.* **2016**, *670*, 1−11.
(58) Zevalkink, A.; Takagiwa, Y.; Kitahara, K.; Kimura, K.; Snyder, G. J. Thermoelectric Properties and Electronic Structure of the Zintl Phase $Sr_5Al_2Sb_6$. *Dalton Trans.* **2014**, *43* (12), 4720.
(59) Wubieneh, T. A.; Wei, P. C.; Yeh, C. C.; Chen, S.; Chen, Y. Y. Thermoelectric Properties of Zintl Phase Compounds of $Ca_{1-x}Eu_xZn_2Sb_2$ ($0 \leq x \leq 1$). *J. Electron. Mater.* **2016**, *45* (3), 1942−1946.
(60) Ogunbunmi, M. O.; Baranets, S.; Childs, A. B.; Bobev, S. The Zintl Phases $AIn_2As_2$ ($A$ = Ca, Sr, Ba): New Topological Insulators and Thermoelectric Material Candidates. *Dalton Trans.* **2021**, *50* (28), 9173−9184.
(61) Wood, M.; Aydemir, U.; Ohno, S.; Snyder, G. J. Observation of Valence Band Crossing: The Thermoelectric Properties of $CaZn_2Sb_2$-$CaMg_2Sb_2$ Solid Solution. *J. Mater. Chem. A* **2018**, *6* (20), 9437−9444.
(62) Wolf, M.; Hinterding, R.; Feldhoff, A. High Power Factor vs. High ZT—A Review of Thermoelectric Materials for High-Temperature Application. *Entropy* **2019**, *21* (11), 1058.


https://doi.org/10.1021/acs.inorgchem.1c02209
*Inorg. Chem.* XXXX, XXX, XXX−XXX